









Temperature dependence of the local electromagnetic field at the Fe site in multiferroic bismuth ferrite

T. T. Dang ^{1,*}, J. Schell ^{1,2}, A. G. Boa ³, D. Lewin ¹, G. Marschick ⁴, A. Dubey,¹ M. Escobar-Castillo,¹ C. Noll ⁵, R. Beck,⁵ Dmitry V. Zybakin,⁶ K. Glukhov,⁷ I. C. J. Yap ⁸, A. Mokhles Gerami,⁹ and D. C. Lupascu ¹

¹*Institute for Materials Science and Center for Nanointegration Duisburg-Essen (CENIDE),*

University of Duisburg-Essen, 45141 Essen, Germany

²*European Organization for Nuclear Research (CERN), CH-1211 Geneva, Switzerland*

³*Technical University of Denmark (DTU), 2800 Kongens Lyngby, Denmark*

⁴*Institute of Solid State Electronics & Center for Micro- and Nanostructures, TU Wien, Vienna 1040, Austria*

⁵*Helmholtz-Institut für Strahlen- und Kernphysik, University of Bonn, 53115 Bonn, Germany*

⁶*Chair Materials for Electrical Engineering and Electronics, Institute of Materials Science and Engineering, Institute of Micro and Nanotechnologies MacroNano, TU Ilmenau, Gustav-Kirchhoff-Strasse 5, 98693 Ilmenau, Germany*

⁷*Institute for Physics and Chemistry of Solid State, Uzhhorod National University, 88000 Uzhhorod, Ukraine*

⁸*Universität Göttingen, Fakultät für Physik, Friedrich-Hund-Platz 1, 37077 Göttingen, Germany*

⁹*School of Particles and Accelerators, Institute for Research in Fundamental Sciences (IPM), P.O. Box 19395-5531, Tehran, Iran*



(Received 11 March 2022; revised 21 June 2022; accepted 5 July 2022; published 11 August 2022)

In this paper, we present a study of the temperature-dependent characteristics of electromagnetic fields at the atomic scale in multiferroic bismuth ferrite (BiFeO₃ or BFO). The study was performed using time differential perturbed angular correlation (TDPAC) spectroscopy on implanted ¹¹¹In (¹¹¹Cd) probes over a wide temperature range. The TDPAC spectra show that substitutional ¹¹¹In on the Fe³⁺ site experiences local electric polarization, which is otherwise expected to essentially stem from the Bi³⁺ lone pair electrons. Moreover, the TDPAC spectra show combined electric and magnetic interactions below the Néel temperature T_N . This is consistent with simulated spectra. X-ray diffraction (XRD) was employed to investigate how high-temperature TDPAC measurements influence the macroscopic structure and secondary phases. With the support of *ab initio* DFT simulations, we can discuss the probe nucleus site assignment and can conclude that the ¹¹¹In (¹¹¹Cd) probe substitutes the Fe atom at the B site of the perovskite structure.

DOI: [10.1103/PhysRevB.106.054416](https://doi.org/10.1103/PhysRevB.106.054416)

I. INTRODUCTION

Multiferroic materials exhibit more than one of the primary ferroic properties in the same phase. The relevant properties include ferromagnetism (FM), ferroelectricity, and ferroelasticity. Over the past decades, multiferroic materials have attracted increasing attention due to their potential for various practical applications in technology. Within the group of materials that exhibit these characteristics, there is a large focus on research [1] regarding BiFeO₃ (BFO), as both its Néel and Curie temperatures are well above room temperature (RT; $T_N \approx 370^\circ\text{C}$ [1] and $T_C \approx 820^\circ\text{C}$ [2]). Previous investigators have shown that BFO exhibits both magnetism and particularly strong ferroelectricity at RT and thus might be implemented and utilized effectively in various electronic devices such as sensors, memory, and spintronic and

photovoltaic devices. This indicates the potential for future BFO-related innovations [1].

The magnetoelectric (ME) effect in BFO results from a distortion in the perovskite structure that is part of the BFO macrostructure. The Goldschmidt tolerance factor (t) is one of the many possible ways to describe the extent of this distortion. When this ratio is <1 , as with BFO ($t = 0.88$, with Bi³⁺ in eightfold coordination, Fe³⁺ in sixfold coordination, and high spin [1]), the oxygen octahedra must contort to fit into a cell that is too small. For bulk BFO, the tilting angle δ of the oxygen octahedra is $\sim 13.8^\circ$ around the polar [111] axis and is directly related to the Fe-O-Fe angle θ , which is $\sim 154.1^\circ$ [3]. These angles are shown clearly in Fig. 1, which was reproduced based on the work of Ruchi *et al.* (Fig. 1) [3] using the VESTA program [4]. The distortion along the [111] direction arises from the lone pair, where the s^2 electrons from the Bi hybridize with the p electrons from oxygen to induce ferroelectricity [5]. Moreover, the Fe-O-Fe angle is important because it controls both the magnetic exchange and orbital overlap between Fe and O and thus determines the magnetic ordering temperature and conductivity [1].

According to the literature [1,6], the crystal structure of BFO in the α phase is the rhombohedral $R3c$ space group with the hexagonal cell parameters $a = 5.58 \text{ \AA}$ and

*thien.dang@uni-due.de

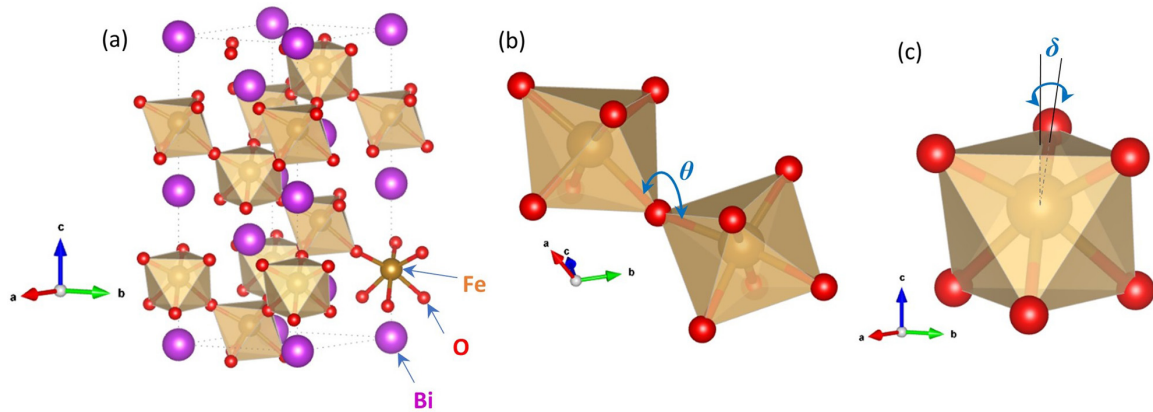


FIG. 1. (a) Unit cell representation of BFO where the Bi-O bonds are not shown. (b) Magnified view of two neighboring, interconnected FeO_6 octahedra. (c) FeO_6 octahedra viewed along the threefold axis to emphasize octahedral tilting. This picture was reproduced based on the work of Ruchi *et al.* (Fig. 1) [3] using the VESTA program [4].

$c = 13.87 \text{ \AA}$ at RT. The stability of this phase can be divided into two nonoverlapping temperature regions, with the Néel temperature T_N as the boundary line. Below T_N , which includes RT, BFO exhibits antiferromagnetic (AFM) properties. Above T_N , and up to the Curie temperature T_C , BFO is in the paramagnetic state. Around T_C , a ferroelectric-paraelectric phase transition appears in the β phase. This causes an abrupt contraction in the sample volume. Marschick *et al.* [2] have noted that the symmetry of the β -phase crystal structure is orthorhombic β -BFO with the $Pbnm$ space group. Before BFO undergoes this ferroelectric transition, it undergoes a large spontaneous polarization ($P \approx 90\text{--}100 \mu\text{C cm}^{-2}$) [5,7] in the pseudocubic [111] direction. This direction is also the axis of rotation for octahedral tilting. The spontaneous polarization along the [111] axis transforms the $Pbnm$ space group (β phase) [2] (which corresponds to an ideal cubic perovskite) into the rhombohedral $R3m$ group (α phase). The main aims of this paper are (1) to investigate coupling between electric and magnetic interactions at temperatures below T_N and (2) to characterize the α and β phases by evaluating the evolution of hyperfine interaction parameters with temperature.

II. EXPERIMENTAL DETAILS

Polycrystalline BFO ceramic samples were synthesized from a stoichiometric mixture of finely powdered bismuth oxide (Bi_2O_3 , 99.9% Acros Organics) and iron oxide (Fe_2O_3 , 99.99% Alfa Aesar). After calcination for 3 h at 820°C , the powder was compressed into pellets and sintered again for 6 h in air at 820°C [2]. The resulting samples were then ion-implanted at an energy of 80 keV and incidence angle of 10° at the Bonn Radioisotope Separator and Implanter (BONIS) facility in Bonn, Germany [8]. More information about the implantation process and the BONIS facility can be found in the literature [8,9]. Additional ^{111}In implantations were performed at the Ion Separator OnLine DEvice-European Organization for Nuclear Research (ISOLDE-CERN) [10] at 30 keV. The implantation depth was simulated using the Stopping and Range of Ions in Matter software [11] based

on a density of 8.34 g/cm^3 . The estimated ion implantation depth is 221 \AA . Since time differential perturbed angular correlation (TDPAC) spectroscopy measures only the local surroundings around the probe nucleus, this depth implies that the sample surface is not accounted for in the measurements unless the ^{111}In (^{111}Cd) probe diffuses outwards and reaches the surface during high-temperature measurements. Since the beam sweeping technique is employed during the implantation process, the probe is distributed homogeneously along the implanted face of the sample and not concentrated in one portion. Therefore, it is possible to cut the BFO pellet into different pieces that could be measured in different TDPAC spectrometers simultaneously. This enables a study of how the duration of TDPAC experiments performed at high temperatures influence the results. It is well known that secondary phases are formed at high temperatures, but these were not detected during previous TDPAC experiments performed with ^{111m}Cd [2], which took ~ 3 h for each temperature point. Measurements performed using the ^{111}In (^{111}Cd) probe take longer. The last measurements before the complete decay of the probe required especially long measurement durations. Specifically, for KATAME, the first measurement was taken at 650°C for 4 h. This was followed by high-temperature measurements in ascending order until the temperature slightly reached above the Curie temperature point, reaching 835°C . The last temperature measurements were carried out in descending order from 600°C until RT. A similar measuring procedure was taken for K1, but the first two measurements were performed at 800 and 840°C (12 h for each measurement). We have aimed to start measuring at high temperatures to remove damages caused by the implantation process and to investigate the effect on the spectra that are caused by the BFO decomposition. Almost every damage could be removed after a 20 min measurement at such high temperatures.

After the ^{111}In implantation, the sample was shipped to ISOLDE-CERN [10] where the full TDPAC study took place within the department of ISOLDE solid state physics [12]. Two TDPAC spectrometers were employed for the measurements: one digital apparatus named KATAME [13] and one analogue apparatus named K1 [14].

X-ray diffraction (XRD) measurements of the sample were performed before ion implantation and a second time after TDPAC spectrometry, using an Empyrean Series 2 XRD setup (PANalytical). Using a copper K_{α} x ray of wavelength $\lambda = 1.54 \text{ \AA}$ and incident x-ray angles of 5° to 45° , the x-ray penetration lengths in the BFO sample, which were calculated using the software HIGHSCORE PLUS [15], are between 2.2 and 17.7 \mu m . In this paper, XRD measurements are used to evaluate the effects of long-duration TDPAC measurements performed at high temperatures on the composition of BFO.

III. TDPAC FORMALISM AND SIMULATIONS

Detailed descriptions of the TDPAC technique and its formalism can be found in the literature [16–19]. In this paper, we focus on presenting the TDPAC formalism for combined hyperfine interactions (CHIs).

In principle, two γ rays emitted consecutively from the same nucleus can be detected by two detectors arranged either perpendicular to each other or in opposite directions. Upon considering all possible combinations of detector positions in 4- and 6-detector arrangements, respectively, one finds that 12 and 30 single-coincidence spectra can be generated. In each coincidence spectrum, the background due to accidental coincidences is subtracted, allowing the experimental count rate ratio $R(t)$ to be obtained, which describes the deviation between the coincidence count rates of the 180° and 90° orientations of the two detectors [20]:

$$R(t) = 2 \frac{W(180^{\circ}, t) - W(90^{\circ}, t)}{W(180^{\circ}, t) + 2W(90^{\circ}, t)} = A_{22}^{\text{eff}} G_{22}(t), \quad (1)$$

where $W(180^{\circ}, t)$ denotes the fourth or sixth root of the product of the 180° spectra after background subtraction and zero-point adjustment. Here, $W(90^{\circ}, t)$ denotes the 8th or 24th root of the product of the 90° spectra from the 4- or 6-detector setups, respectively. Also, A_{22}^{eff} is the experimental anisotropy coefficient of the γ_1 - γ_2 cascade and $G_{22}(t)$ is the theoretical perturbation factor, whose form depends on the type of hyperfine interaction induced at the probe site.

The perturbation factor $G_{22}(t)$ for pure electric and pure magnetic interactions is discussed fully in the work of Butz [18]. The perturbation factor $G_{22}(t)$ for CHIs has the following form [21]:

$$G_{22}(t) = a_0 + \sum_{n=1}^{30} a_n \cos(\omega_n t). \quad (2)$$

In Eq. (2), ω_n are transition frequencies taken from 30 nondiagonal elements of a 6×6 frequency matrix; a_n are taken from 30 nondiagonal elements of a 6×6 amplitude matrix and are amplitudes of 30 corresponding transition frequencies; a_0 is determined from the sum of six diagonal elements of the amplitude matrix and is called the hard-core value. We note that Eq. (2) is valid only for the case where CHIs occur at one probe site, and damping caused by local environmental distortion and the temporal resolution of the detector is not considered.

When several fractions of nuclei subjected to different hyperfine interactions are found in the same sample and damping and the temporal resolutions of the detectors are considered,

the effective perturbation factor is given by [22,23]:

$$G_{22}(t) = \sum_{i=1}^m f_i \left(a_{0i} + \sum_{n=1}^{30} a_{ni} \cos(\omega_{ni} t) \right) \times \exp\{-0.5[(\delta_i \omega_{ni} t)^p + (\omega_{ni} \tau_R)^2]\}, \quad (3)$$

where f_i is the fraction of probe atoms exposed to the hyperfine interaction i ($i = 1, 2, 3, \dots$), with $\sum_{i=1}^m f_i = 1$. The damping of fraction i [the distribution of the electric field gradient (EFG) or interaction frequency], δ_i , shows the extent of angular distortion of the local environment around the probe. The values $p = 1$ and 2 in the exponent represent Lorentzian and Gaussian distributions respectively. Here, τ_R is the finite time resolution (full width at half maximum) of the detectors. The distribution width can be written in the form $\exp[-0.5(\delta_i \omega_{ni} t)^p]$ or $\exp[-\frac{1}{p}(\delta_i \omega_{ni} t)^p]$ [22,24]. We use the first form here, as shown in Eq. (3).

In the presence of a fluctuating hyperfine field, Eq. (3) is multiplied by the exponential term $\exp(-\lambda_i t)$ to give

$$G_{22}(t) = \sum_{i=1}^m f_i \left(a_{0i} + \sum_{n=1}^{30} a_{ni} \cos(\omega_{ni} t) \right) \times \exp\{-0.5[(\delta_i \omega_{ni} t)^p + (\omega_{ni} \tau_R)^2]\} \exp(-\lambda_i t), \quad (4)$$

where λ_i is the exponential decay constant or dynamic transition [22]. The amplitudes a_{ni} and transition frequencies ω_{ni} can be derived from the CHI Hamiltonian matrix for spin $I = \frac{5}{2}$. They depend significantly on the asymmetry parameter η (which represents the deviation of the EFG from axial symmetry) and the Euler angles β and γ (which give the relative orientation of the magnetic field direction with respect to the principal EFG axes in the electric coordinate system) [25]. The complete process of calculating a_{ni} and ω_{ni} can be found in the work of Catchen [21].

We fitted the TDPAC spectra using Eq. (4). From the fits, we can extract various hyperfine parameters such as the quadrupole interaction frequency caused by the electric quadrupole splitting and the Larmor frequency caused by the magnetic dipole splitting of the intermediate state. The quadrupole interaction frequency strongly depends on the asymmetry parameter (η), which is presented explicitly in the works of Butz [18] and Marschick *et al.* [2]. In addition to the hyperfine interaction frequencies, other hyperfine interaction parameters such as the asymmetry parameter (η), the frequency distribution (δ), and the Euler angles (β and γ) are extracted from the fit. These extracted parameters reveal information about the nature of the hyperfine interactions of the materials in question.

In this paper, the TDPAC spectra for purely electric interactions ($T > T_N$) were fitted using the GFIT19 software package, a modified version of the NNFIT software package [26,27]. The TDPAC spectra for combined electric magnetic hyperfine interactions were fitted using PACFIT software [28]. To ensure that all hyperfine interaction parameters extracted from the fit are mathematically consistent with the theoretical

model outlined earlier in this section, we generated artificial TDPAC signals from the CHI model with our experimentally obtained hyperfine parameters as inputs and with the assistance of Mathematica [29]. These generated TDPAC spectra were then compared with our experimentally obtained TDPAC signals so that similarities and differences could be identified. These simulations are designed for measurements on polycrystalline, multiferroic sources and partially follow

$$\begin{bmatrix} 10 + \frac{5}{2}y\cos\beta & \frac{\sqrt{5}}{2}y\sin\beta(\cos\gamma - i\sin\gamma) & \sqrt{10}\eta & 0 & 0 & 0 \\ \frac{\sqrt{5}}{2}y\sin\beta(\cos\gamma + i\sin\gamma) & -2 + \frac{3}{2}y\cos\beta & \sqrt{2}y\sin\beta(\cos\gamma - i\sin\gamma) & 3\sqrt{2}\eta & 0 & 0 \\ \sqrt{10}\eta & \sqrt{2}y\sin\beta(\cos\gamma + i\sin\gamma) & -8 + \frac{1}{2}y\cos\beta & \frac{3}{2}y\sin\beta(\cos\gamma - i\sin\gamma) & 3\sqrt{2}\eta & 0 \\ 0 & 3\sqrt{2}\eta & \frac{3}{2}y\sin\beta(\cos\gamma + i\sin\gamma) & -8 - \frac{1}{2}y\cos\beta & \sqrt{2}y\sin\beta(\cos\gamma - i\sin\gamma) & \sqrt{10}\eta \\ 0 & 0 & 3\sqrt{2}\eta & \sqrt{2}y\sin\beta(\cos\gamma + i\sin\gamma) & -2 - \frac{3}{2}y\cos\beta & \frac{\sqrt{5}}{2}y\sin\beta(\cos\gamma - i\sin\gamma) \\ 0 & 0 & 0 & \sqrt{10}\eta & \frac{\sqrt{5}}{2}y\sin\beta(\cos\gamma + i\sin\gamma) & 10 - \frac{5}{2}y\cos\beta \end{bmatrix} \quad (5)$$

The Hamiltonian matrix in Eq. (5) depends on four parameters: y , η , β , and γ . Each Hamiltonian matrix element is written in units of $\hbar\omega_Q$. The parameter y is defined as the ratio of the Larmor frequency (ω_L) to the quadrupole frequency (ω_Q), i.e., $y = \omega_L/\omega_Q$, and represents the strength of the magnetic field relative to the electric field. According to conventional definitions, the strengths of the magnetic and electric interactions are equal when $y = 3$ for integer I and $y = 6$ for half-integer I [30,31].

The first TDPAC spectrum simulations in the electric coordinate system, which were pioneered by Boström *et al.* [25], only produced results for the case of the Euler angle $\gamma = 0$. Our team performed these calculations for TDPAC spectra and their corresponding fast Fourier transforms (FFTs) for nonzero Euler angles ($\gamma \neq 0$) in the electric coordinate system.

Figure 2 presents the simulated TDPAC spectra and their corresponding FFTs for CHIs at one probe site without damping caused by local environmental distortion and the temporal resolution of the detectors. We plotted graphs of sim-

ulated TDPAC spectra with increasing relative magnetic field strengths y , varying asymmetry parameters (η), and constant Euler angles γ and β of 30° . TDPAC spectral modulation is greater at higher magnetic field strengths. This phenomenon can be seen visually in the corresponding FFT spectra, where the transition frequency peaks increase with y . Moreover, the FFT spectra for higher y values exhibit more nonoverlapping peaks than those for low y values. This is due to the nonlinear way the eigenvalue increases with respect to y , as described in Fig. 3. Our results displayed in the last three spectra of Fig. 2 (for $\gamma = 0$) are compatible with those of Boström *et al.* (Fig. 4) [25].

IV. RESULTS AND DISCUSSIONS

A. TDPAC results

1. Electric quadrupole interactions above T_N (from 370 to 835 °C)

The probe site experiences pure electric quadrupole interactions in this temperature range, allowing us to characterize the phase transition from the α phase (rhombohedral phase) to

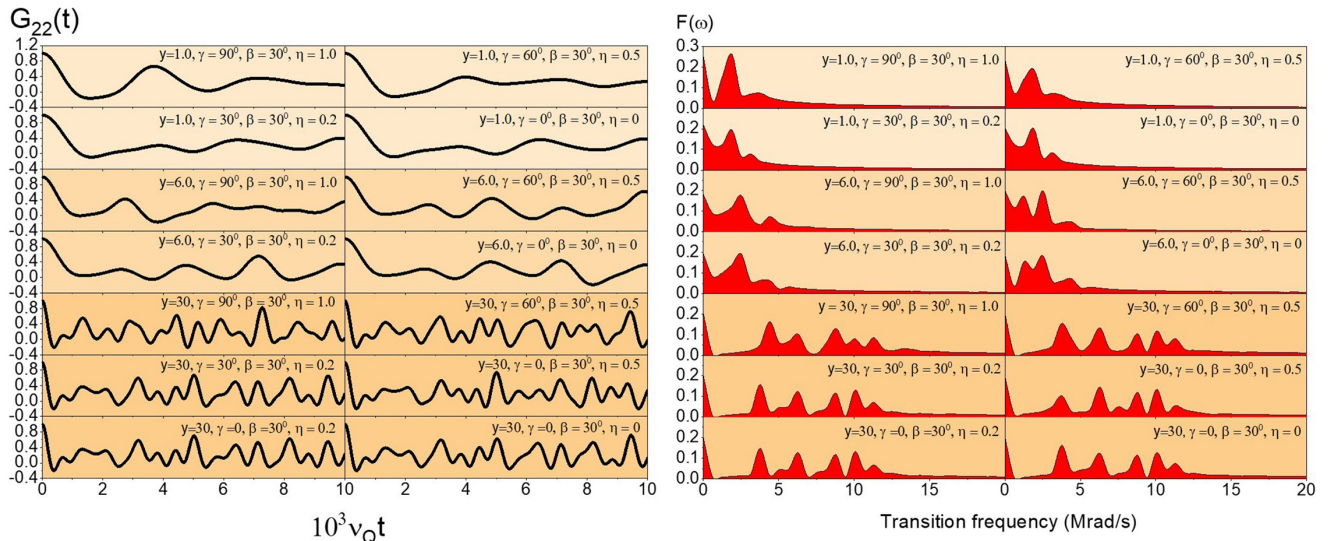


FIG. 2. Simulated time differential perturbed angular correlation (TDPAC) spectra of combined hyperfine interactions in the electric coordinate systems (left) and their corresponding fast Fourier transforms (FFTs; right).

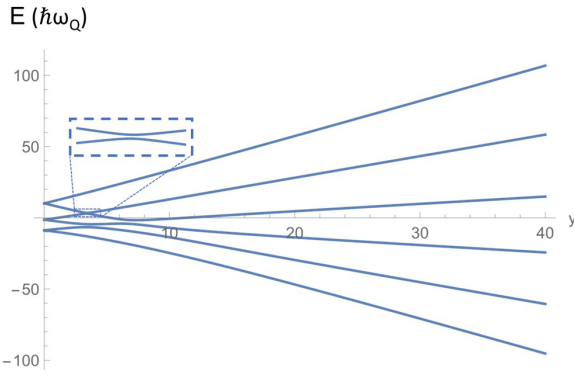


FIG. 3. The eigenvalues of the combined hyperfine interaction Hamiltonian are plotted as functions of y , with $\gamma = 60^\circ$, $\beta = 30^\circ$, and $\eta = 0.5$, in the electric coordinate system. Note that the eigenvalues are in units of $\hbar\omega_Q$.

the β phase (orthorhombic phase). We visually note changes in the shapes and characteristics of the $R(t)$ spectra in Figs. 5 and 6 once the measuring temperature crosses the Curie temperature T_C ($T_C = 835^\circ\text{C}$ for KATAME and $T_C = 829^\circ\text{C}$ for K1, exhibiting the different calibrations of the setups). In Fig. 4, the sharp decrease in the value of ω_Q at $T \sim 829^\circ\text{C}$ is displayed at the transition from the α to the β phase, yielding the Curie temperature from our experiments to be around this temperature point ($T_C \approx 829^\circ\text{C}$). The sudden frequency drop is also proof of the existence of a first-order phase transition from the α to the β phase in BFO. The Curie temperature obtained here is slightly different from that in the literature ($T_C \approx 820^\circ\text{C}$) [2] for various possible reasons. (1) It is noted that the temperature of the BFO phase transition is dependent on the particle size. This effect is also observed for the Néel temperature T_N and was studied using Mössbauer spectroscopy [32]. Furthermore, the work of Mazumder *et al.* [33] reported that the phase transition

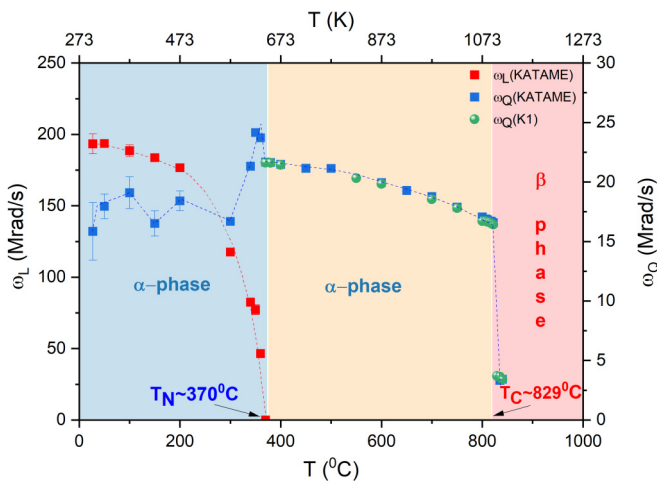


FIG. 4. Temperature dependence of the quadrupole (ω_Q) and Larmor (ω_L) frequencies according to the KATAME and K1 machines. The α phase is shown in orange ($T > T_N$) and light blue ($T < T_N$) layers, whereas the β phase is shown in the brick red layer. The red and blue dotted curves are shown for visual guidance.

feature varies with the particle size, and the feature near the Néel temperature T_N becomes more prominent. The Néel temperature $T_N \sim 380^\circ\text{C}$ was determined in their work [33], which is 10°C higher than the corresponding value recorded in the literature [1]. Similar behavior might happen with the Curie temperature in this paper, which is 9°C higher than the recorded value in the literature ($T_C \approx 820^\circ\text{C}$) [2]. (2) The furnace used for high-temperature measurements has an uncertainty of $\pm 5^\circ\text{C}$. The α - β phase transition temperature offset between the K1 and KATAME machines falls within the mentioned uncertainty. (3) The longer measurement times and thus thermal treatments may slightly affect the transition to the β phase. In fact, long duration of measurements has inadvertently created a secondary phase ($\text{Bi}_2\text{Fe}_4\text{O}_9$), which will be thoroughly discussed in Sec. IV D. The existence of $\text{Bi}_2\text{Fe}_4\text{O}_9$ can affect the transition temperature in bismuth ferrite.

The clear difference between the EFGs of the α and β phases is visualized via the quadrupole transition frequencies and their symmetry. As presented in the FFT spectra, EFG_α is symmetric, while EFG_β is not. As shown in the FFTs of EFG_α , the ratio of transition frequencies $\omega_1:\omega_2:\omega_3$ is 1:2:3, as expected. This is consistent with the small value of the asymmetry parameter ($\eta \approx 0$) shown in Fig. 7. The origin of this small asymmetry parameter is the symmetrical charge distribution around the probe in the absence of internal magnetic field. Furthermore, these transition frequencies remain unchanged regardless of whether a digital (KATAME) or analog (K1) TDPAC spectrometer is used for the measurements.

The α - β phase transition is also visible in the evolution of the asymmetry parameter (η) and damping (δ) with the measurement temperatures shown in Figs. 7 and 8. The crystal structure exhibits a drastic change in symmetry that matches the EFG values observed in the FFTs. The value of η is close to 0 in the α phase, but η increases and approaches unity in the β phase. This unusual behavior of the asymmetry parameter (η) is typically expected during a transition from rhombohedral $R3c$ to orthorhombic $Pbnm$ [6]. Thus, the iron site in BFO undergoes a phase change from a highly symmetric state to a highly asymmetric state. The small asymmetry parameter observed for the α phase and small damping ($< 2\%$) are due to small lattice imperfections [34] like the counterrotations of adjacent oxygen octahedra about the [111] axis [1,7]. They reflect the great sensitivity of the ^{111}In (^{111}Cd) probe to deviations from axial symmetry while it is incorporated in a dilute regime in BFO. Furthermore, small damping (δ) values indicate a narrow EFG distribution, which enables accurate analysis. These small values do not vary within the rhombohedral phase but start to increase when the structure shifts toward the orthorhombic phase.

Moreover, the obtained spectra do not show signs of the appearance of secondary phase $\text{Bi}_2\text{Fe}_4\text{O}_9$ [35], which should form at high temperatures due to the volatility of Bi_2O_3 [6]. This does not imply that the secondary phase is absent but rather that the TDPAC technique does not detect it under the present measurement conditions.

2. CHIs (from 340 to 360 °C)

In this temperature range, we can see a complete phase transition once the temperature passes through the Néel

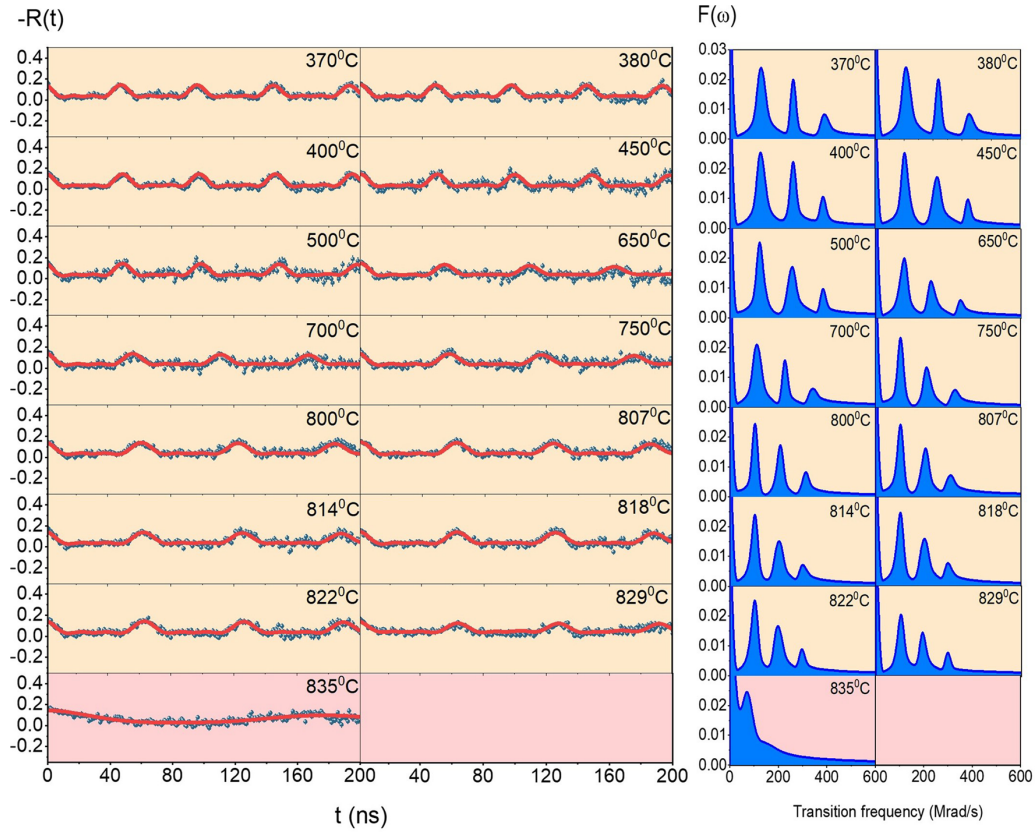


FIG. 5. (left) KATAME perturbed angular correlation (PAC) spectra at various measurement temperatures (370–835 °C) and (right) the corresponding fast Fourier transforms (FFTs). The α phase is shown in orange layers, whereas the β phase is shown in the brick red layer.

temperature $T_N \approx 370$ °C, below which the TDPAC spectra show CHIs. Figure 9 shows TDPAC spectra for the CHI at the probe ^{111}In site and their corresponding FFTs at various measurement temperatures from RT to 360 °C (blue background). The AFM phase transition can be seen at 370 °C and is characterized by changes in shape of the TDPAC spectra and FFTs. Coupling between the electric and magnetic fields is also characterized by changes in the Larmor and quadrupole frequencies with the measurement temperature, as shown in Fig. 4. The ratio of the Larmor frequency ω_L to the quadrupole frequency ω_Q near T_N is < 4 [$y = \omega_L/\omega_Q < 4$ ($y \approx 12$ at RT)]. This means that the magnetic field becomes weaker than the electric field at the ^{111}In site in BFO near the transition temperature. The weaker interaction modulates the dominant interaction. This can be seen in the TDPAC spectra for the CHI (Figs. 2 and 9). For CHIs, the FFTs (Fig. 9) should show 15 peaks that correspond to 15 transition frequencies. However, only 6–8 transition frequencies with the highest amplitudes are observed in this paper. The other transition frequencies, which exhibit low amplitudes, cannot be distinguished in the FFTs.

The temperature dependences of ω_L and ω_Q follow different trends in which ω_L decreases with temperature and follows a power law trend, while ω_Q fluctuates near the transition point T_N . In Fig. 10, the evolution of the Larmor frequency with respect to the measurement temperature is described by Eqs. (6) and (7):

$$\omega_L(\tau) = \omega_L(0)Q_{5/2}(\tau)\sqrt{1-\tau}, \quad (6)$$

with

$$\begin{aligned} Q_{5/2}(\tau) = & 1 + 0.508037\tau + 0.813671\tau^2 - 4.26886\tau^3 \\ & + 9.01576\tau^4 - 9.75394\tau^5 \\ & + 5.36827\tau^6 - 1.19731\tau^7, \end{aligned} \quad (7)$$

and $\tau = \frac{T}{T_c}$.

Equations (6) and (7) are derived from the analytical solution for the Weiss equation for FM for $S = \frac{5}{2}$, as shown in eqs. (42) and (49) in the work of Barsan and Kuncser [36]. They provide a good estimate of the temperature dependence of spontaneous magnetization in the entire interval $0 < \tau < 1$. A maximum relative deviation is $< 1.5 \times 10^{-3}$ for $\tau \approx 0.1$; for larger values of τ , the approximation is much better. A thorough discussion of the exact and approximate analytical solutions to the Weiss FM equation can be found in eqs. (42)–(49) of Barsan and Kuncser [36]. We note that Weiss's theory is originally conceived for the case of FM. However, it is also noted that the theory is equally applicable to the case of AFM, as the predictions for AFM are quite like those for FM [37]. The Néel temperature extracted from the fitting is $T_N = 370.5 \pm 1.3$ °C (643.5 ± 1.3 K), which agrees well with the literature value $T_N \approx 370$ °C (643 K), as determined in the work by Catalan and Scott [1]. This paper includes measuring the DC resistivities of good-quality bulk BFO samples. The list of results for the Néel temperature of BFO, determined using various experimental methods, is presented in Table I.

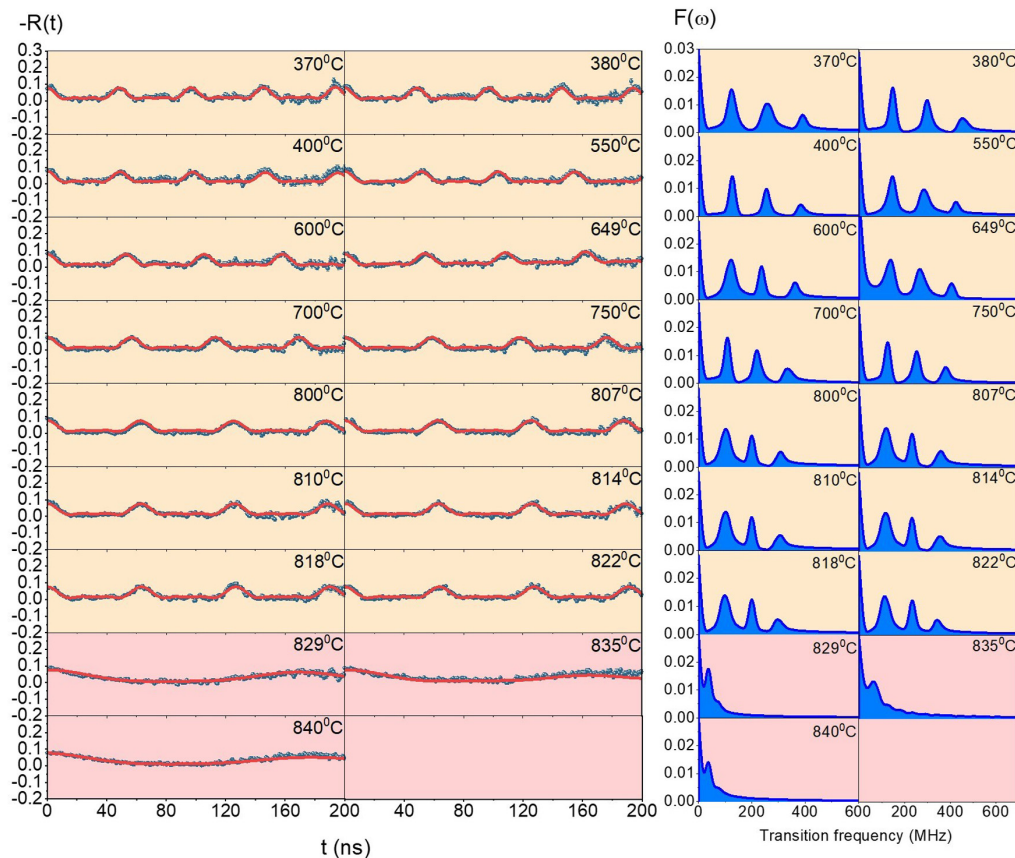


FIG. 6. (left) K1 perturbed angular correlation (PAC) spectra at various measurement temperatures (370–840 °C) and (right) the corresponding fast Fourier transforms (FFTs). The α phase is shown in orange layers, whereas the β phase is shown in the brick red layer.

The anomalous behaviors of the temperature dependences of the quadrupole frequency and asymmetry parameter, which are observed close to the magnetic transition temperature in Figs. 4 and 7, can be attributed to strong coupling between magnetic, electric, and elastic properties in BFO. The elastic instability that results from distortion of the oxygen coordination may be correlated with local short-range magnetic ordering, which is G-type AFM [35]. A magnetoelastic instability then occurs, and local distortions, which break the axial symmetry, appear as channels for magnetic frustration. This phenomenon can be observed in other multiferroic compounds such as $\text{Pr}_{1-x}\text{Ca}_x\text{MnO}_3$, AgCrO_2 , $\text{Bi}_2\text{Fe}_4\text{O}_9$, and $\text{Bi}_2\text{Mn}_4\text{O}_{10}$ [35,38,39]. This frustration can be reduced by the spontaneous magnetostriction effect, which describes the deformation of the FM specimen during magnetization [40]. The origin of spontaneous magnetostriction in BFO is conjectured to be like that in $\text{Bi}_2\text{Fe}_4\text{O}_9$, caused by the displacement of Fe ions that modifies its equilibrium positions and hence induces oxygen coordination distortions [35].

The CHI is also characterized by the asymmetry of EFG (η), which follows the same trend as ω_L . That is, it decreases in the temperature region below T_N . The strength of the magnetic field that acts on the probe site is positively but nonlinearly correlated with the value of the asymmetry parameter. This implies that the presence of a locally strong magnetic field (≈ 14 T at RT) might cause tilting of the octahedral structure around the probe site, breaking the lattice symmetry

around the probe and thus altering the symmetry of the charge distribution around the probe. Therefore, the presence of a stronger magnetic field corresponds to the observation of a less symmetrical EFG around the probe. The low damping value ($< 0.5\%$; Fig. 8) indicates that the hyperfine interaction frequencies are well defined, and few local distortions are induced around the probe.

The most robust fitting parameter in our data is the angle between the EFG orientation, namely, the z axis of the respective local principal axis coordinate system of the diagonalized tensor, and the local magnetic field direction, given by the Euler angle β [25] (not to be confused with the Landau coefficient β). According to neutron scattering data [41], the location of the magnetic cycloid of BFO can reside in the easy planes $\{112\}$, which are formed by the ferroelectric polar direction $\langle 111 \rangle_{\text{cubic}}$ and the propagation vector of the cycloid in the $\langle 110 \rangle_{\text{cubic}}$ direction (these two directions are perpendicular). Figure 11 illustrates two possible easy planes for magnetization and one direction of \vec{P} at the Fe site in the BFO pseudocubic unit cell. For a positive V_{zz} , which determines the positive z axis of the principal coordinate system of the EFG tensor, the local magnetic field is angled at $\beta \approx 120^\circ$ with respect to this z axis, slightly larger than the crystallographic angle of 109.5° , as shown in Figs. 11 and 12. This value of β is compatible with the one obtained from our former study for strong ME coupling in BFO using ^{181}Hf tracers [42]. If the z axis shows along $-\vec{P}$, then the direction

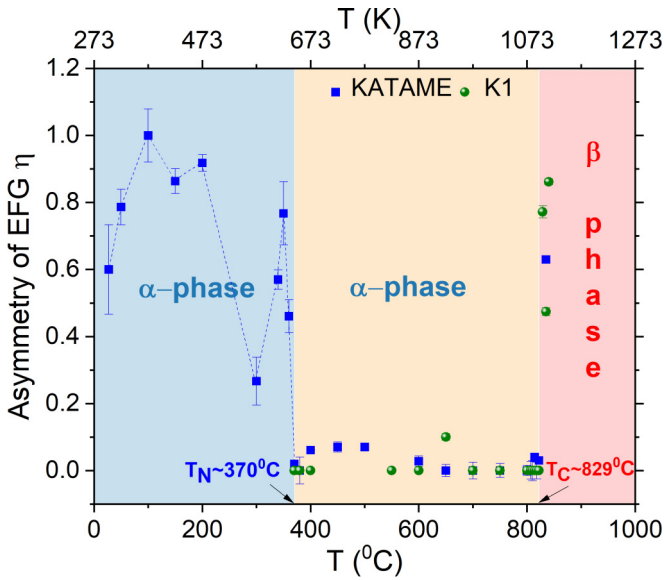


FIG. 7. Temperature dependence of the asymmetry parameter (η) according to KATAME and K1. The α phase is shown in orange ($T > T_N$) and light blue ($T < T_N$) layers, whereas the β phase is shown in the brick red layer. The blue dotted curve is shown for visual guidance.

of $\vec{M}_{\text{eff,local}}$ will be reversed but still reside in the same easy plane. In our previous paper on the ^{181}Hf probe, there were two potential fits to the data. In the first, two easy planes of magnetization yield two different combined magnetic-electric interactions for the probes yielding two effective sites. This was the finally assumed configuration. The second fit of nearly

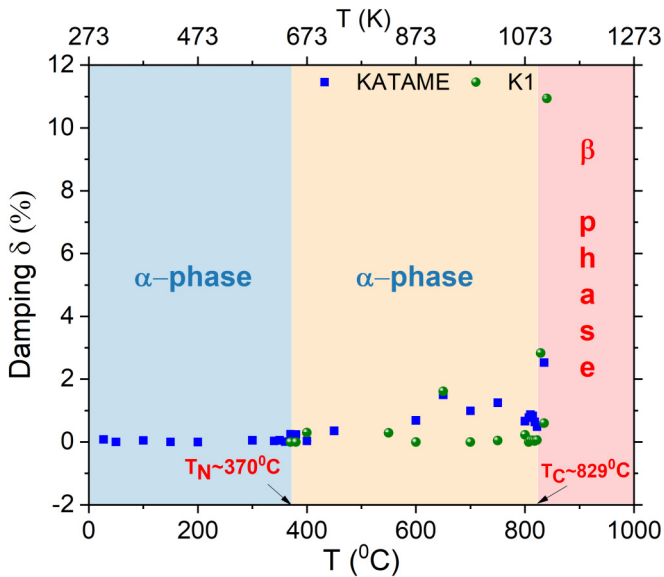


FIG. 8. Temperature dependence of the damping parameter (δ) for KATAME and K1. The α phase is shown in orange ($T > T_N$) and light blue ($T < T_N$) layers, whereas the β phase is shown in the brick red layer.

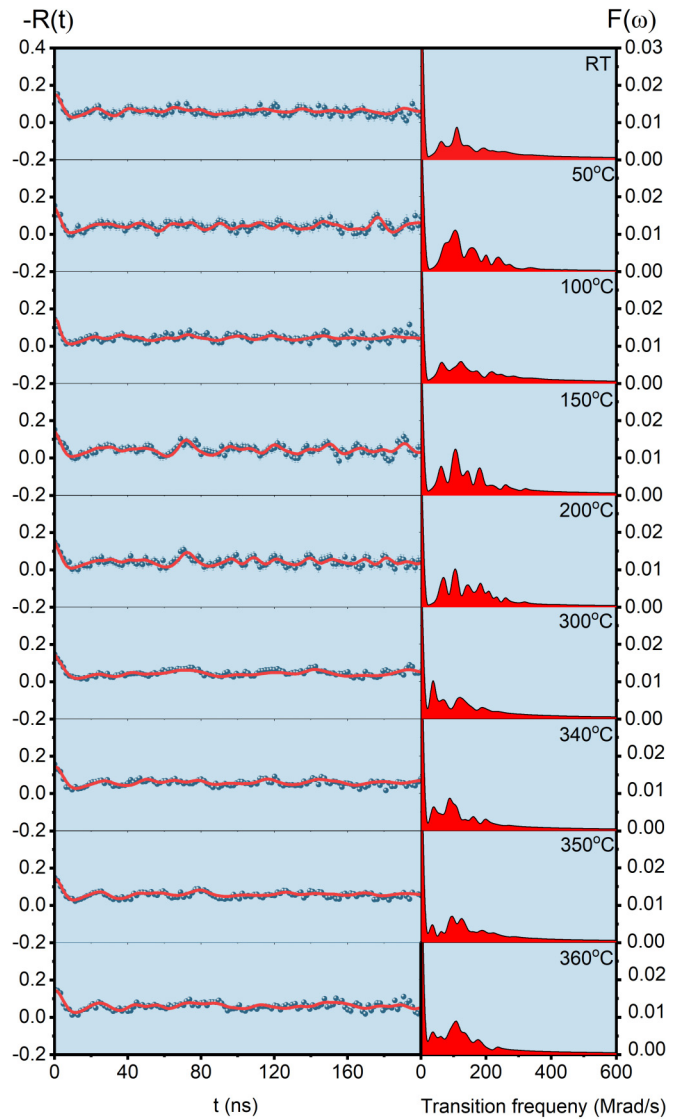


FIG. 9. (left) KATAME perturbed angular correlation (PAC) spectra at various measurement temperatures [room temperature (RT) = 360 °C] and (right) the corresponding fast Fourier transforms (FFTs).

the same fitting certainty (χ^2) assumed only one single angle between EFG orientation and magnetization direction. In the present set of fits using ^{111}In , only one angle between the EFG axis and the effective local magnetic field is found. Thus, our PAC results are in good agreement with the final assumption by Lebeugle *et al.* [41] that there is a preferred orientation of magnetization with respect to polarization. The angle β is almost unchanged with temperature. The foreign atom In appears to preferably stabilize a certain magnetic direction over the other. This can have remarkable implications on the role of dopants in stabilizing certain magnetic states in BFO. Near T_N , the fits are more unstable, which might relate to the magnetic frustration happening near the magnetic phase transition. In addition to β , the other Euler angle γ [25], which determines the rotational angle of magnetic coordinate system in the electric coordinate system, is found to be $\sim 45^\circ$, as shown in Fig. 12.

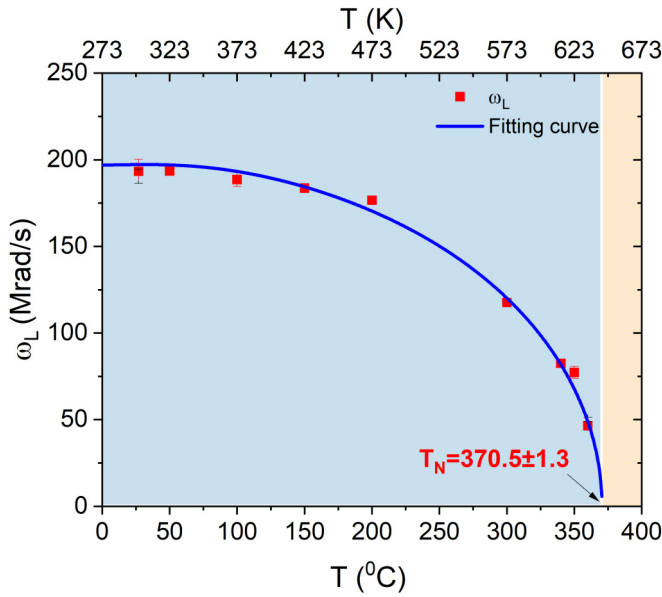


FIG. 10. Temperature dependence of the Larmor frequencies. The fitting function is derived from the analytical solution of the Weiss equation as shown in Eqs. (6) and (7).

According to the Dzyaloshinskii-Moriya interaction, the G-type AFM order in BFO is slightly canted and does not fully cancel. Two canted (AFM) spins yield a vector sum magnetization, which is very small and oscillates with the same periodicity as the spin cycloid. This sum component is nearly perpendicular to the overall spin orientations of the cycloid within the easy planes. If the ^{111}In (^{111}Cd) probe would experience this effective sum field, it would have to be oriented under 90° with respect to the polar axis and the cycloid propagation direction. In this paper, however, we do not observe 90° , which is consistent with our previous research on BFO using ^{181}Hf as a probe [42]. Therefore, the selection of a particular spin state near the ^{111}In (^{111}Cd) probe ion is certainly independent of the second-order Dzyaloshinskii-Moriya interaction and directly correlated with the primary order parameter, namely, the spins of the AFM sublattice itself.

TABLE I. List of results for the Néel temperature of BFO, as determined using various experimental techniques. This table is updated from the work of Fischer *et al.* [43].

T_N (K)	Experimental technique	Reference
~ 650	Neutron diffraction	[44]
640	Neutron diffraction	[45]
640 ± 5	Mössbauer effect	[46]
598–617	Thermal expansion (x rays)	[47]
654.9	Mössbauer effect	[48]
650	Magnetic susceptibility	[49]
595 ± 15	Neutron diffraction	[43]
625 ± 10	Magnetic susceptibility	[43]
643	DC resistivity	[1]
643.5 ± 1.3	TDPAC	This paper

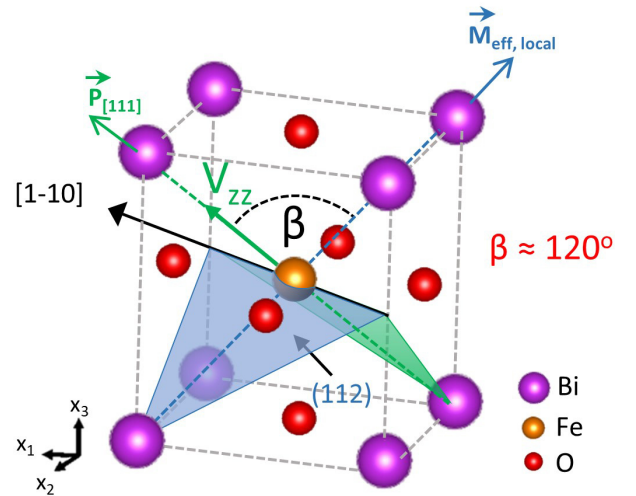


FIG. 11. Configuration for polarization direction, effective magnetic field direction and cycloid orientation in BFO pseudocubic unit cell as resulting from our data. This figure was made based on the source [42].

In the PACFIT software, the combined-interaction Hamilton matrix is written in the electric coordinate system. To verify whether the formalism used by PACFIT is consistent with the formalism described in the methodology section (Sec. III) of this paper, we calculate the artificial TDPAC signal via Mathematica using the parameters extracted from our fits of the TDPAC measurements done by PACFIT. The results from Mathematica are compatible with PACFIT, as shown in Fig. 13. The calculation shows that the PACFIT software is consistent with the formalism described in Sec. III and can be used to fit TDPAC spectra to analyze CHIs.

B. XRD results

The XRD measurements are separated into two phases, with the first half measured right after the synthesis of the

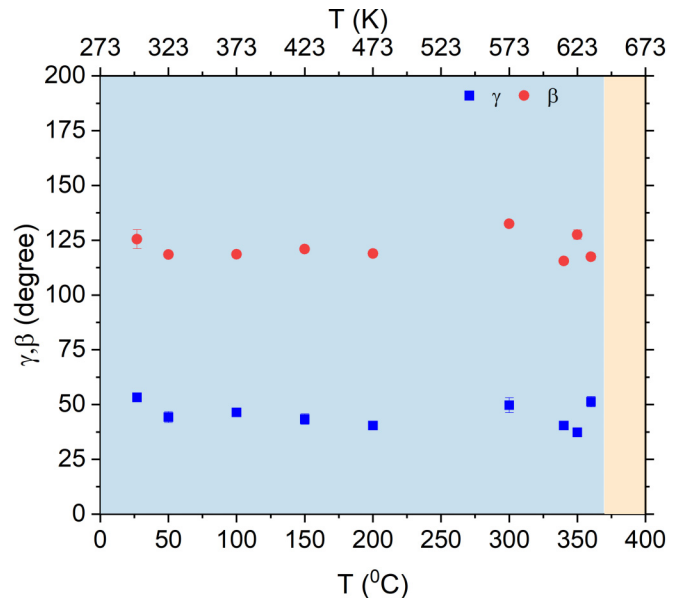


FIG. 12. Euler angles γ and β .

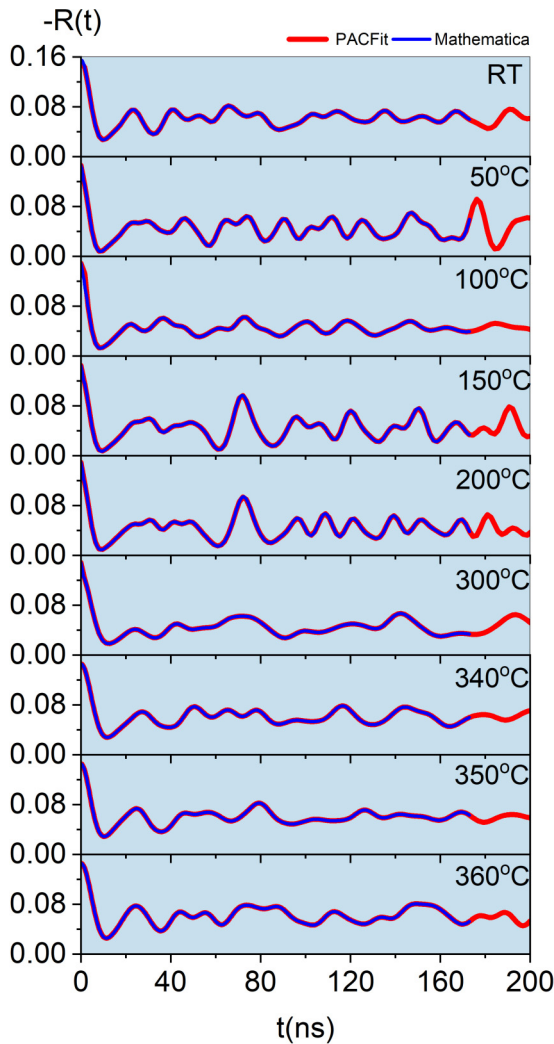


FIG. 13. Comparison of the Mathematica calculations and the fittings performed using PACFIT for our perturbed angular correlation (PAC) measurements at various temperatures. The red curves are plotted up to 170 ns intentionally to note the degree of overlap between the artificial time differential PAC (TDPAC) spectra and our experimental fits.

sample and thus before the TDPAC measurements and the second half measured after the TDPAC measurements, when the sample pieces have already undergone the thermal treatment. For our measurements, it is also necessary to distinguish between the samples used with KATAME and K1 setups, as the thermal treatments used for the two samples during the TDPAC measurements are different. The Rietveld phase analysis was performed using the HIGHSCORE PLUS software [15].

1. XRD measurements before TDPAC

Once the BFO ceramic sample was synthesized using the solid-state method, it was measured via XRD to analyze its purity. The result can be observed in Fig. 14. Here, it can be seen visually that the calculated value expected for the pure BFO sample agrees with the experimental data result and matches well with standard Inorganic Crystal Structure

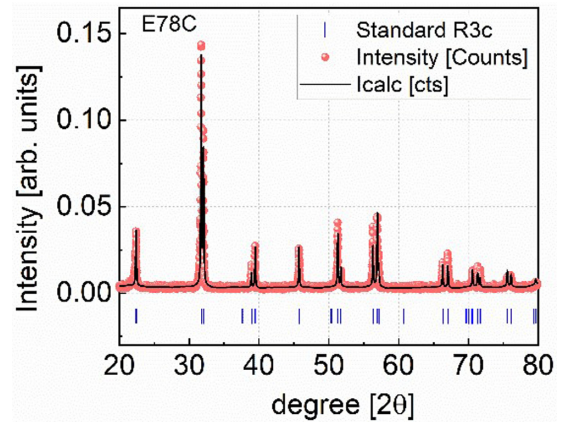


FIG. 14. X-ray diffraction (XRD) spectrum of BFO at room temperature, before the time differential perturbed angular correlation (TDPAC) measurements.

Database (ICSD) code for R3c: 98-007-5324. This indicates that there are no significant secondary phases present in the sample before TDPAC measurements under XRD detection limit.

2. XRD after TDPAC

The XRD measurements performed after TDPAC were done to investigate the formed secondary phases in the sample. Figures 15(a) and 15(b) show that the secondary phase $\text{Bi}_2\text{Fe}_4\text{O}_9$ in *Pbam* symmetry is present in both samples (*Pbam* ICSD code: 98-026-2861) but in different quantities. The thermal treatment is longer in the sample used with the K1 TDPAC spectrometer, and the results show that the percentage of secondary phase in this sample is greater than in the sample measured using the KATAME TDPAC spectrometer. For the K1 sample, the pure BFO and $\text{Bi}_2\text{Fe}_4\text{O}_9$ contents are 75.1 and 24.9%, respectively. For the KATAME sample, these values are 80.3 and 19.7%, respectively, as confirmed via Rietveld analysis. Thus, we can see qualitatively that the thermal treatment duration affects the amount of secondary phase formed in the sample directly.

With an x-ray penetration depth of 2.2–17.7 μm , the XRD results suggest that the BFO secondary phase can form and diffuse much deeper into the sample than the ^{111}In (^{111}Cd) probe. However, the secondary phase was not detected via TDPAC measurements because apparently its signal is too small. The In (^{111}Cd) probe might be located at the Fe site in $\text{Bi}_2\text{Fe}_4\text{O}_9$, but the number of events is not sufficient for visibility in the PAC spectrum.

C. Data interpretation and comparison with literature

There was a similar TDPAC study of BFO that was carried out in the ISOLDE facility using the same probe ^{111}Cd but arising from the decay product of parent nucleus ^{111m}Cd [2]. The intermediate level used to sense the hyperfine interactions is the same for both ^{111}In (^{111}Cd) and ^{111m}Cd (^{111}Cd). The most significant difference between ^{111m}Cd (^{111}Cd) and ^{111}In (^{111}Cd) when they are implanted into BFO is that ^{111m}Cd (^{111}Cd) is located at the A site of BFO and substitutes bismuth atoms, whereas ^{111}In (^{111}Cd) is located at the B site of BFO

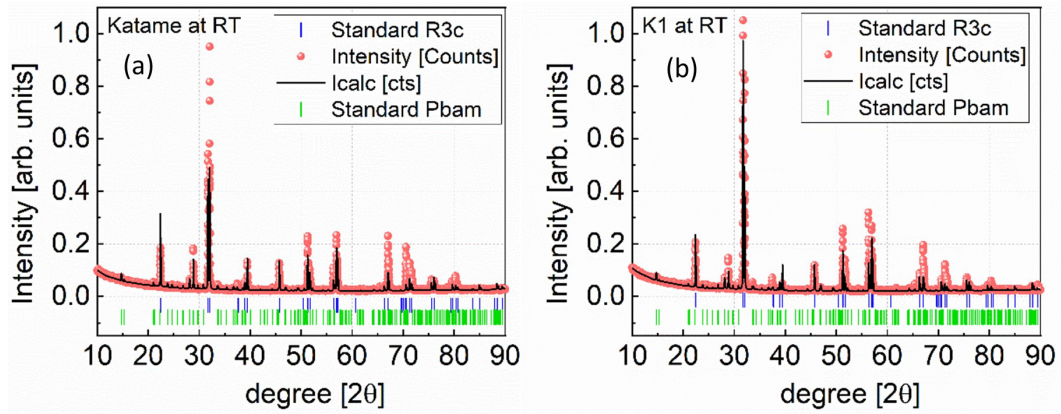


FIG. 15. X-ray diffraction (XRD) measurements at room temperature after time differential perturbed angular correlation (TDPAC) for (a) KATAME and for (b) K1.

and substitutes iron atoms. The location of the ^{111}In (^{111}Cd) probe at the iron site is confirmed via density function theory (DFT) simulations and matches physicochemical assignments using ionic radii, which will be thoroughly discussed. The ^{111m}Cd -BFO research team used DFT simulations performed via the Vienna *Ab initio* Simulation Package. The results of these simulations can be found in table I of Marschick *et al.* [2]. These results can also be used to analyze BFO (^{111}In), as both probes share the same intermediate nuclear state. The simulations show that the values of the hyperfine parameters of the Cd probe substituting the iron atoms in β -BFO are close to our results [$V_{zz} \approx 2.37/8.43(10^{21}/\text{Vm}^2)$, $\eta \approx 0.87/0.18$, $\omega_0 \approx 33.3-35.9(\text{Mrad/s})$]. Hence, the ^{111}In (^{111}Cd) probe is located at the Fe site of BFO.

When comparing TDPAC measurements of the same type of material using different probe nuclei, the quadrupole interaction frequency is the reference hyperfine parameter. It reveals the electrical environment and thus the site in the sample in which the probe nucleus sits. Figure 16 depicts the quadrupole interaction frequencies for both the BFO (^{111}In) and BFO (^{111m}Cd) studies with respect to temperature. For the α phase of BFO, the quadrupole interaction frequency is higher for ^{111}In than for ^{111m}Cd . This implies that the electric interaction is stronger at the Fe site than that at the Bi site. Moreover, the quadrupole frequency drops drastically to 20 Mrad/s for the β phase in BFO (^{111}In). In ^{111m}Cd , the quadrupole frequency increasingly tends toward a value of ~ 110 Mrad/s instead. The significant difference in quadrupole interaction frequencies among the two studies is attributed to the fact that, for BFO (^{111}In), the V_{zz} component of the EFG follows Landau theory, but Landau theory fails to explain the V_{zz} trend in BFO (^{111m}Cd). The V_{zz} in BFO (^{111}In) follows the parabolic trend in the region where the α phase is dominant. This trend is fitted using the derived equation found in Landau theory (Fig. 17), in which we extract the expression for the dependence of the EFG on spontaneous polarization of the crystal up to T_C [42,50]:

$$V_{zz} = \xi P_s^2 = \xi \frac{\beta}{2\gamma} \left[1 + \sqrt{\frac{1}{4} - \frac{\chi_0^{-1}\gamma}{\beta^2} (T - T_C)} \right]. \quad (8)$$

The Landau expansion coefficients $\alpha = \chi_0^{-1}(T_0 - T)$, β , and γ are defined according to the convention in the literature [50]. The temperature dependence of α is expressed in terms of the absolute temperature (T) and the Curie-Weiss point T_0 (not to be mistaken for the Curie temperature T_C , for which a first-order transition is given by $T_C = T_0 + \frac{3}{16} \frac{\beta^2}{\chi_0^{-1}\gamma}$ [50]). The local EFG at the probe site is a result of the change in polarization. The change in polarization with respect to temperature is related to the change in V_{zz} . Equation (8) is used to fit the graph of the V_{zz} of BFO (^{111}In) in the α phase against the measurement temperature. The parameters of the fit are shown in Table II. From this, we can deduce that V_{zz} at the Fe site is directly proportional to P_s^2 via the relation $V_{zz}^{\text{Fe}} = \xi P_s^2 \approx 9 \times 10^{18} P_s^2$, and the linear dependence of the local EFGs on the square of spontaneous polarization is shown in the inset of Fig. 17. This is in good agreement with Landau theory.

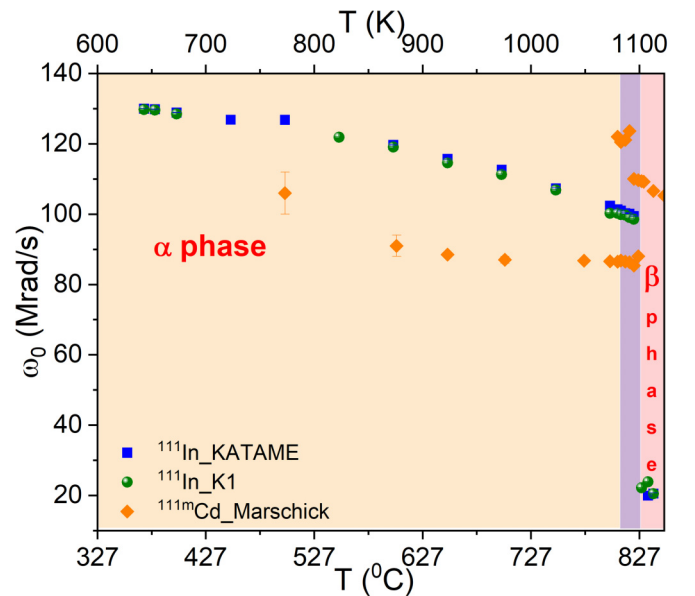


FIG. 16. Quadrupole interaction frequencies for BFO (^{111}In) and BFO (^{111m}Cd). The phase transition disorder interval is displayed in purple.

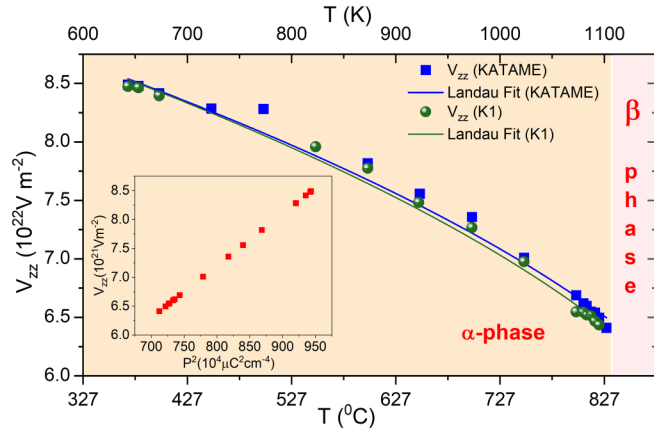


FIG. 17. Temperature dependence of V_{zz} for KATAME and K1 and a fit produced using Landau theory. The inset shows linear dependence of local electric field gradients (EFGs) on the square of polarization.

This is an indication that the ^{111}In (^{111}Cd) probe can measure the change in the polarization of BFO, thus the deformation of the electron cloud of the adjacent Bi ions. It is expected that the polarization mostly stems from the Bi site [5,7], but we cannot discard the possibility of a small contribution to polarization from the Fe site. The physics behind the different values of the hyperfine parameters, which depend on the probe location, is discussed in the work of Arnold *et al.* [6]. We

TABLE II. Parameters produced by Landau fitting for the KATAME and K1 processes.

Parameter	KATAME	K1
ξ (Vm^2/C^2)	$9 \times 10^{18} \pm 2 \times 10^{16}$	$9 \times 10^{18} \pm 2 \times 10^{16}$
$\frac{\beta}{\gamma}$ [$(\text{C}/\text{m}^2)^2$]	960	964
$\frac{\chi_0^{-1}}{\beta}$ [$(\text{C}/\text{m}^2)^2/\text{K}$]	1.45	1.52
T_c (K)	1102	1095
T_c ($^\circ\text{C}$)	829	822

pay attention to Fig. 4 of Arnold *et al.* [6], where it is noted that the bond lengths are short for Bi-O. This indicates that the atoms always lie closely. For Fe-O, three of the bond lengths are squeezed, and the other three are elongated. Since the behavior of the ionic bonds is different, the results are expected to be clearly different as well.

Marschick *et al.* [2] also concluded that a phase transition disorder interval exists between the α and β phases [purple background in Figs. 16 and 18(b)] in the 804–829 $^\circ\text{C}$ temperature range. However, TDPAC measurements conducted with ^{111}In (^{111}Cd) do not show signs of the mentioned transition interval. Figure 18(b) shows the BFO (^{111m}Cd) spectra, in which the top graph $T = 800^\circ\text{C}$ shows the pure spectrum of the α phase. In the middle graph ($T = 822^\circ\text{C}$), the spectrum starts to change as the Bi coordination is now disordered. This is a signal of α - β phase transition. In the bottom graph ($T = 831^\circ\text{C}$), the β phase is reached fully. Thus, the structure is unaltered again and has the space group $Pbmn$. However, Fig. 18(a) shows the BFO (^{111}In) spectra produced using K1. Here, the top graph shows the pure spectrum of the α phase of BFO, and the bottom graph shows the pure spectrum of the β phase. However, the middle graph does not show an α - β phase transition. Instead, the signal still corresponds to the α phase. As described in Sec. IV A, where the entire set of BFO (^{111}In) spectra is analyzed, there is a clear distinction between these two phases. This is especially true in the measurement region from 829 to 835 $^\circ\text{C}$, where the spectra show the pure β phase. Comparison of the two spectra indicates that the transition between the phases is first order when ^{111}In (^{111}Cd) is used as a probe, whereas a disorder interval exists between the α and β phases when ^{111m}Cd (^{111}Cd) is used. Two hypotheses are given for the presence of this interval. The first conjecture comes from local coordination disorder of the Bi atoms. The coordination of bismuth with respect to oxygen changes from sixfold in the α phase to eightfold in the β phase. The changes in the coordination (Bi-O) and bond lengths in the Bi-O and Fe-O octahedra are illustrated in Fig. 19. However, the coordination numbers of the iron and oxygen atoms do not change with temperature. Thus, the phase transition interval cannot be seen in our results, given that ^{111}In (^{111}Cd) is on the B site. The second explanation comes from the presence of polytype

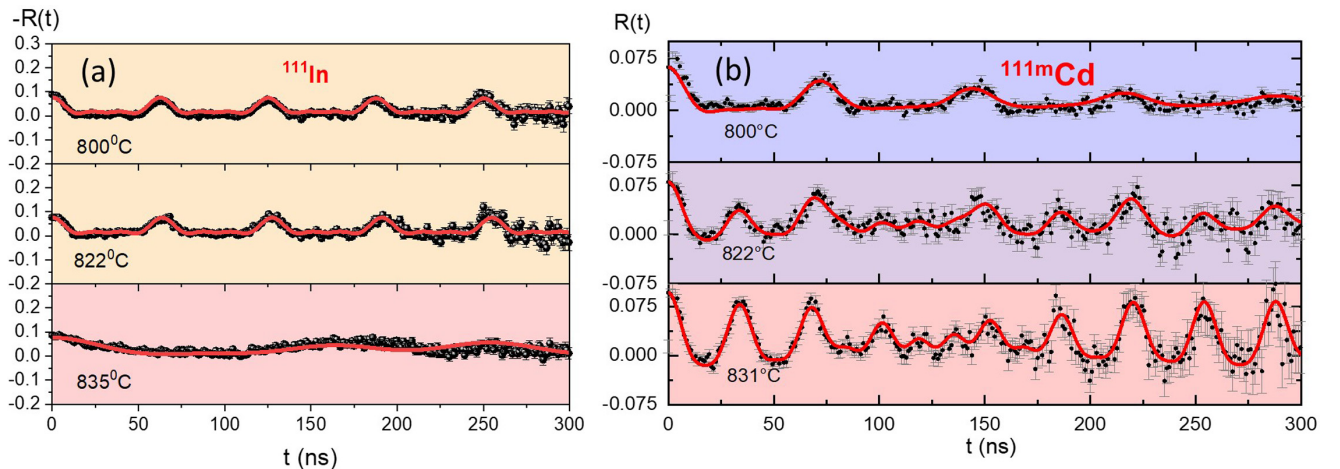


FIG. 18. $R(t)$ spectra comparing the α - β phase transition of (a) BFO (^{111}In) and (b) BFO (^{111m}Cd).

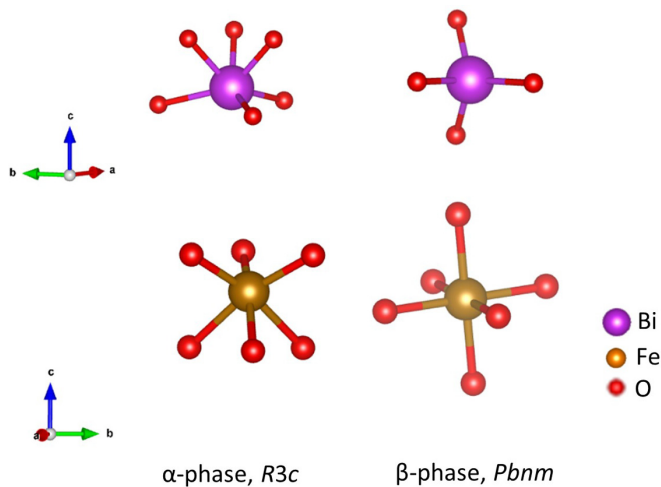


FIG. 19. Changes in the coordination and ion bond lengths of Bi-O (top) and changes in the bond lengths of Fe-O (bottom) with the phase transition from $R3c$ to $Pbnm$ symmetry. Made with VESTA [4].

phases that act as intermediate structures between the α and β phases.

D. Probe site assignment

The location of the In ion in the BFO lattice sites has been discussed in several papers [51,52]. Research that consists of a study of In-doped BFO nanoparticles [51] is discussed briefly here. They sought to improve the multiferroic properties of BFO via the cation size effect, for it is known that substitution of bismuth atoms in BFO for rare earth ions improves the desired properties. This is consistent with the conjecture that the indium ions substitute the bismuth ions due to the smaller ionic radius of ^{111}In [53] and because both In^{3+} and Bi^{3+} are nonmagnetic ions. The findings of their research included the conclusion that the indium ions occupy the bismuth site in BFO, although they mainly used the XRD technique and were restricted to the α phase. It is certain from our results that the ^{111}In (^{111}Cd) probe does not occupy the A site in the BFO structure. Moreover, sixfold coordinated In^{3+} has an ionic radius of 80 pm, which is closer to the ionic radius of Fe^{3+} (64.5 pm) than to that of Bi^{3+} (103 pm) [53]. From the above information, we conjecture that In^{3+} is located at the B site in BFO.

Another comprehensive study on substitutional doping in BFO was performed by Gebhardt and Rappe [52]. Substitutional dopants cause structural changes in the BFO structure. There is a direct effect from substituting ions of different sizes. There are also secondary effects from oxidation (p -type doping) or reduction (n -type doping) of the iron centers, which cause changes in the oxygen octahedra. Therefore, relaxation of the lattice cannot be explained by only the differences in ionic radii. Rather, it is related mainly to oxidation of the iron and the decreased spatial requirements of the FeO_6 octahedra. Highly oxidized cations in oxidation states of +3 and above prefer the B site for most of the periodic table until the sixth period, i.e., up to cations that are almost as large as Bi^{3+} itself. Since indium is part of the fifth period in the periodic table, it

is among the cations that prefer to substitute the B site of BFO. Furthermore, indium is part of group XIII, which contains elements that form +3 ions by donating valence s and p electrons to the oxygen valence band. In group XIII, only Tl^{3+} is large enough to prefer A-site substitution [52]. Furthermore, fig. 9 in Gebhardt and Rappe [52] shows a graph that lists the site preferences for substitutional dopants in BFO. The negative and positive areas correspond to the A and B sites, respectively. In^{3+} tends to prefer the B site and substitute iron atoms. However, In^{3+} is shown at the boundary that divides the site occupation preferences; thus, it has no preference for either A or B sites. Concrete site assignments then depend on other thermodynamic or structural factors. Our PAC data prove that the probe is located at the B site.

V. CONCLUSIONS

In this paper, we use TDPAC spectroscopy to probe the local environment around the implanted nuclear probe ^{111}In (^{111}Cd) in bismuth ferrite. The measurements were performed at various temperatures. Two TDPAC spectrometers were used for the purpose of reproducibility. The results from the two spectrometers agree well. These measurements, when compared with *ab initio* simulations from previous research [2], indicate that the nuclear probe is located at the B site of the BFO structure, which corresponds to the substitution of iron atoms. The results from the $R(t)$ spectra, which show a first-order transition that corresponds to a change in crystal structure from $R3c$ in the α phase to $Pbnm$ in the β phase, agree with the above mentioned assessment. Furthermore, we note that the octahedral structure formed by the iron and oxygen atoms in BFO does not change in coordination number as the crystal structure of BFO is altered globally from the α to the β phase. Thus, the ^{111}In (BFO) TDPAC spectroscopy result does not include any coordination disorder intervals. The ^{111}In (^{111}Cd) probe can measure the change in the local polarization of α -phase BFO even if it is located at the Fe site, and the evolution of local polarization with temperature obeys the Landau theory.

The TDPAC study of ^{111}In (BFO) below the Néel temperature shows that the coupling between electric and magnetic interactions exists at the Fe site. Due to the good fitting process, the magnetic signal is well separated from the electric signal, and its strength decreases with temperature and becomes zero at $T_N \approx 370^\circ\text{C}$. The temperature dependence of the magnetic dipole frequency strictly follows the solution to the Weiss equation. Moreover, magnetic frustration resulting from magneto-elastic instability occurs near the magnetic phase transition T_N , reflected by the abnormal behaviors of the quadrupole frequency and the asymmetry parameter of the EFG. The relative orientation of the effective magnetic field direction with respect to the principal axis of the EFG is $\sim 120^\circ$ and exhibits instability near the Néel temperature T_N due to magnetic frustration. The appearance of only one angle rather than the two possible by symmetry of the crystal may imply a certain stabilization of a certain magnetic preferred orientation for certain dopants. Here, In seems to behave somewhat different from Hf. Final conclusions on this effect will need further study using other probes.

ACKNOWLEDGMENTS

Financial support was provided by the Federal Ministry of Education and Research (BMBF) through Grants No. 05K16PGA and No. 05K19SI1, alongside support from the ISOLDE collaboration. In addition, support was provided by the European Union's Horizon 2020 Framework research and innovation program under Grant Agreement No. 654002 (ENSAR2) given to the ISOLDE experiment

(IS647). DFG (Deutsche Forschungsgemeinschaft) for financial support through the Project LU 729/21-1 (Project Number 396469149) is highly acknowledged. We greatly appreciate their financial contributions and support, which led to the publication of this paper. We thank the ISOLDE team deeply for their support during the TDPAC measurements. We thank Dr. Matthias Nagl for the technical support given during the use of PACMASTER software.

- [1] G. Catalan and J. F. Scott, Physics and applications of bismuth ferrite, *Adv. Mater.* **21**, 2463 (2009).
- [2] G. Marschick, J. Schell, B. Stöger, J. N. Gonçalves, M. O. Karabasov, D. Zybakin, A. Welker, M. Escobar C., D. Gaertner, I. Efe *et al.*, Multiferroic bismuth ferrite: perturbed angular correlation studies on its ferroic α - β phase transition, *Phys. Rev. B* **102**, 224110 (2020).
- [3] R. Tomar, N. Wadehra, V. M. Gaikwad, and S. Chakraverty, Low field manifestation of spiral ordering in sheet like BiFeO₃ nanostructures, *AIP Adv.* **8**, 085306 (2018).
- [4] K. Momma and F. Izumi, VESTA 3 for three-dimensional visualization of crystal, volumetric and morphology data, *J. Appl. Crystallogr.* **44**, 1272 (2011).
- [5] S. R. Burns, O. Paull, J. Juraszek, V. Nagarajan, and D. Sando, The experimentalist's guide to the cycloid, or noncollinear antiferromagnetism in epitaxial BiFeO₃, *Adv. Mater.* **32**, 2003711 (2020).
- [6] D. C. Arnold, K. S. Knight, F. D. Morrison, and P. Lightfoot, Ferroelectric-Paraelectric Transition in BiFeO₃: Crystal Structure of the Orthorhombic β Phase, *Phys. Rev. Lett.* **102**, 027602 (2009).
- [7] J. B. Neaton, C. Ederer, U. V. Waghmare, N. A. Spaldin, and K. M. Rabe, First-principles study of spontaneous polarization in multiferroic BiFeO₃, *Phys. Rev. B* **71**, 014113 (2005).
- [8] K. Freitag, A facility for ion implantation in samples colder than 0.5 k, *Radiat. Eff.* **44**, 185 (1979).
- [9] J. Schell, D. C. Lupascu, A. W. Carbonari, R. D. Mansano, I. S. R. Junior, T. T. Dang, I. Anusca, H. Trivedi, K. Johnston, and R. Vianden, Ion implantation in titanium dioxide thin films studied by perturbed angular correlations, *J. Appl. Phys.* **121**, 145302 (2017).
- [10] R. Catherall, W. Andreazza, M. Breitenfeldt, A. Dorsival, G. J. Focker, T. P. Gharsa, T. J. Giles, J-L. Grenard, F. Locci, P. Martins *et al.*, The ISOLDE facility, *J. Phys. G: Nucl. Part. Phys.* **44**, 094002 (2017).
- [11] J. F. Ziegler, SRIM-2013 software package, <http://www.srim.org>.
- [12] K. Johnston, J. Schell, J. G. Correia, M. Deicher, H. P. Gunnlaugsson, A. S. Fenta, E. David-Bosne, A. R. G. Costa, and D. C. Lupascu, The solid state physics programme at ISOLDE: recent developments and perspectives, *J. Phys. G: Nucl. Part. Phys.* **44**, 104001 (2017).
- [13] M. Nagl, U. Vetter, M. Uhrmacher, and H. Hofsäss, A new all-digital time differential γ - γ angular correlation spectrometer, *Rev. Sci. Instrum.* **81**, 073501 (2010).
- [14] J. Schell, P. Schaaf, and D. C. Lupascu, Perturbed angular correlations at ISOLDE: A 40 years young technique, *AIP Adv.* **7**, 105017 (2017).
- [15] HIGSCORE PLUS, Version 4.7 (4.7.0. 24755), PANalytical B.V. (2017).
- [16] A. Abragam and R. V. Pound, Influence of electric and magnetic fields on angular correlations, *Phys. Rev.* **92**, 943 (1953).
- [17] H. Frauenfelder and R. M. Steffen, *Alpha-, Beta-, and Gamma-Ray Spectroscopy*, edited by K. Siegbahn (North Holland, Amsterdam, 1966), Vol. 2.
- [18] T. Butz, Analytic perturbation functions for static interactions in perturbed angular correlations of γ -rays, *Hyperfine Interact.* **52**, 189 (1989).
- [19] G. Schatz and A. Weidinger, *Nuclear Condensed Matter Physics—Nuclear Methods and Applications* (John Wiley, Chichester, 1996).
- [20] E. Danielsen, R. Bauer, L. Hemmingsen, M.-L. Andersen, M. J. Bjerrum, T. Butz, W. Troger, G. W. Canters, C. W. G. Hoitink, G. Karlsson *et al.*, Structure of metal site in azurin, Met¹²¹ mutants of Azurin, and stellacyanin investigated by ^{111m}Cd perturbed angular correlation (PAC), *J. Biol. Chem.* **270**, 573 (1995).
- [21] G. L. Catchen, Sensitivity of spin $I = \frac{5}{2}$ perturbed-angular-correlation measurements to combined magnetic-dipole and electric-quadrupole hyperfine interactions, *Hyperfine Interact.* **88**, 1 (1994).
- [22] M. Zacate and H. Jaeger, Perturbed angular correlation spectroscopy—a tool for the study of defects and diffusion at the atomic scale, *Defect and Diffusion Forum* **311**, 3 (2011).
- [23] R. Dogra, A. P. Byrne, and M. C. Ridgway, The potential of the perturbed angular correlation technique in characterizing semiconductors, *J. Electron. Mater.* **38**, 623 (2009).
- [24] M. Foraker, P. R. J. Silva, J. T. P. D. Cavalcante, F. H. M. Cavalcante, S. M. Ramos, H. Saitovitch, E. Baggio-Saitovitch, R. Alonso, M. Taylor, and L. A. Errico, Electric field gradients of CeMIn₅ ($M = \text{Co, Rh, Ir}$) heavy-fermion systems studied by perturbed angular correlations and *ab initio* electronic structure calculations, *Phys. Rev. B* **87**, 155132 (2013).
- [25] L. Boström, E. Karlsson, and S. Zetterlund, Calculation of differential angular correlation factors for non-coaxial electric and magnetic fields, *Phys. Scr.* **2**, 65 (1970).
- [26] N. P. Barradas, NNFIT core program: PAC Manual. Lisbon (1992).
- [27] J. G. Correia, GFIT19 software (2019).
- [28] J. Cavalcante and M. Foraker, PACFIT with Spin selection 2.0.0 (Build 342).
- [29] Wolfram Mathematica 12.2.0.0, [Mathematica.licensing.zim.uni-due.de](https://www.wolfram.com/mathematica/licensing/zim-uni-due.de) (2000).
- [30] K. Alder, E. Matthias, W. Schneider, and R. M. Steffen, Nuclear level splitting caused by a combined magnetic dipole and

- non-axially symmetric electric quadrupole interaction, *Arkiv Fysik* **24**, 9 (1962).
- [31] W. S. K. Alder, E. Matthias, and R. M. Stefen, Influence of a combined magnetic dipole and electric quadrupole interaction on angular correlations, *Phys. Rev.* **129**, 1199 (1963).
- [32] J. Landers, S. Salamon, M. E. Castillo, D. C. Lupascu, and H. Wende, Mössbauer study of temperature-dependent cycloidal ordering in BiFeO₃ nanoparticles, *Nano Lett.* **14**, 6061 (2014).
- [33] R. Mazumder, S. Ghosh, P. Mondal, D. Bhattacharya, S. Dasgupta, N. Das, and A. Sen, Particle size dependence of magnetization and phase transition near T_N in multiferroic BiFeO₃, *J. Appl. Phys.* **100**, 033908 (2006).
- [34] M. Forker, The problematic of the derivation of the electric field gradient asymmetry parameter from TDPAC measurements or Mössbauer spectroscopy in imperfect crystal lattices, *Nucl. Instrum. Methods* **106**, 121 (1973).
- [35] F. E. N. Ramirez, G. A. Cabrera-Pasca, J. Mestnik-Filho, A. W. Carbonari, and J. A. Souza, Magnetic and transport properties assisted by local distortions in Bi₂Mn₄O₁₀ and Bi₂Fe₄O₉ multiferroic compounds, *J. Alloys Compd.* **651**, 405 (2015).
- [36] V. Barsan and V. Kuncser, Exact and approximate analytical solutions of Weiss equation of ferromagnetism and their experimental relevance, *Philos. Mag. Lett.* **97**, 359 (2017).
- [37] P. Hofmann, *Solid State Physics—An Introduction*, 2nd ed. (Wiley-VCH, Weinheim, 2015).
- [38] A. M. L. Lopes, G. N. P. Oliveira, T. M. Mendonça, J. Agostinho Moreira, A. Almeida, J. P. Araujo, V. S. Amaral, and J. G. Correia, Local distortions in multiferroic AgCrO₂ triangular spin lattice, *Phys. Rev. B* **84**, 014434 (2011).
- [39] A. M. L. Lopes, J. P. Araujo, V. S. Amaral, J. G. Correia, Y. Tomioka, and Y. Tokura, New Phase Transition in the Pr_{1-x}Ca_xMnO₃ System: Evidence for Electrical Polarization in Charge Ordered Manganites, *Phys. Rev. Lett.* **100**, 155702 (2008).
- [40] S. Chikazumi, *Physics of Ferromagnetism*, 2nd ed. (Oxford University Press, New York, 1997).
- [41] D. Lebeugle, D. Colson, A. Forget, M. Viret, A. M. Bataille, and A. Gukasov, Electric-Field-Induced Spin Flop in BiFeO₃ Single Crystals at Room Temperature, *Phys. Rev. Lett.* **100**, 227602 (2008).
- [42] J. Schell, M. Schmuck, İ. Efe, T. T. Dang, J. N. Gonçalves, D. Lewin, M. E. Castillo, V. V. Shvartsman, Â. R. G. Costa, U. Köster, R. Vianden, C. Noll, and D. C. Lupascu, Strong magnetoelectric coupling at an atomic non-magnetic electro-magnetic probe in bismuth ferrite, *Phys. Rev. B* **105**, 094102 (2022).
- [43] P. Fischer, M. Połomska, I. Sosnowska, and M. Szymański, Temperature dependence of the crystal and magnetic structures of BiFeO₃, *J. Phys. C: Solid State Phys.* **13**, 1931 (1980).
- [44] S. V. Kiselev, R. P. Ozerov, and G. S. Zhdanov, Detection of magnetic order in ferroelectric BiFeO₃ by neutron diffraction, *Sov. Phys.* **7**, 742 (1963).
- [45] J. M. Moreau, C. Michel, R. Gerson, and W. J. James, Ferroelectric BiFeO₃ x-ray and neutron diffraction study, *J. Phys. Chem. Solids* **32**, 1315 (1971).
- [46] A. Biran, P. A. Montano, and U. Shimony, Mössbauer measurements of BiFeO₃ and BiFeO₃-PbZrO₃ systems, *J. Phys. Chem. Solids* **32**, 327 (1971).
- [47] J. D. Bucci, B. K. Robertson, and W. J. James, The precision determination of the lattice parameters and the coefficients of thermal expansion of BiFeO₃, *J. Appl. Cryst.* **5**, 187 (1972).
- [48] C. Blaauw and F. van der Woude, Magnetic and structural properties of BiFeO₃, *J. Phys. C: Solid State Phys.* **6**, 1422 (1973).
- [49] M. Polomska, W. Kaczmarek, and Z. Pająk, Electric and magnetic properties of (B_{1-x}La_x)FeO₃ solid solutions, *Phys. Stat. Solidi A* **23**, 567 (1974).
- [50] M. E. Lines and A. M. Glass, *Principles and Applications of Ferroelectrics and Related Materials* (Clarendon Press, Oxford, 1977).
- [51] G. S. Arya, R. K. Kotnala, and N. S. Negi, Structural and multiferroic properties of Bi_{1-x}In_xFeO₃ (0 ≤ x ≤ 0.20) nanoparticles, *J. Appl. Phys.* **113**, 044107 (2013).
- [52] J. Gebhardt and A. M. Rappe, Doping of BiFeO₃: a comprehensive study on substitutional doping, *Phys. Rev. B* **98**, 125202 (2018).
- [53] R. D. Shannon, Revised effective ionic radii and systematic studies of interatomic distances in halides and chalcogenides, *Acta Cryst. A* **32**, 751 (1976).